Materials & Design 252 (2025) 113730

Contents lists available at ScienceDirect

Materials & Design

journal homepage: www.elsevier.com/locate/matdes

Mitigating core energy losses in Fe-Si alloys fabricated by direct energy deposition through oxide inclusions and abnormal Goss grain growth

Xiaojun Shen [a,1], Konstantinos A. Liogas [b,c,1], Verner Soh Qun Liang [c], Yung Zhen Lek [d], Fanbo Meng [a], Yiming Shen [a], John E. Huber [b], Roger C. Reed [b,f], Pei Wang [c,e], Alexander M. Korsunsky [b], Christopher H.T. Lee [a,*]

[a] School of Electrical and Electronic Engineering, Nanyang Technological University, 50 Nanyang Avenue, 639798, Singapore
[b] Department of Engineering Science, University of Oxford, Parks Road, Oxford OX1 3BH, United Kingdom
[c] Institute of Materials Research and Engineering, Agency for Science, Technology and Research, 138634, Singapore
[d] School of Mechanical and Aerospace Engineering, Nanyang Technological University, Singapore 639798 Singapore
[e] Engineering Cluster, Singapore Institute of Technology, 519961 Singapore
[f] Department of Materials, University of Oxford, Parks Road, Oxford OX1 3PH, United Kingdom

ARTICLE INFO

Keywords:
Directed energy deposition
Abnormal Goss grain
Oxide inclusions
Eddy current loss

ABSTRACT

In traditional electrical steel production oxide inclusions are conventionally perceived as deleterious elements for the functional and structural properties. The present work describes the fabrication of a high silicon content electrical steel alloy (Fe-6.5wt%Si) using directed energy deposition (DED), coupled with oxide inclusions to mitigate core energy losses. Abnormal Grain Growth (ABG) was observed after thermal post-processing at 1000 °C for 24 h (1000–24), together with the creation of oxide inclusions mainly around the grain boundaries. Magnetic properties were assessed through dynamic and quasi-static measurements for both as-printed (AP) and 1000–24 samples. The quasi-static analysis revealed hysteresis losses of 206.9 J/m^3 for the AP and 19.02 J/m^3 for the 1000–24, with maximum flux densities of 1.295 T and 1.031 T, at the magnetic field of 3000 A/m. Dynamic magnetic analysis demonstrated an improvement of 39.2% in the total core losses of the 1000–24 sample (2088.8 J/m^3), compared to the AP sample (3436.9 J/m^3). The microstructure of the 1000–24 sample revealed the formation of Goss texture via ABG, ultimately decreasing the static hysteresis loss. Furthermore, an improved electrical resistivity compare to conventional electrical steel alloys was demonstrated at 119 μΩcm for the 1000-24 sample, and 105 μΩcm for the AP sample. This work introduces a promising avenue to minimize core energy losses by incorporating oxide inclusions and ABG Goss texture in additively manufactured soft magneitc components after thermal post-processing.

1. Introduction

Electricity plays a vital role in modern society by enabling flexible and distributed power supplies for a wide range of locations and applications, from homes and factories to transportation and communication systems. Consequently, there is an increasing need to develop energy-efficient devices for electric power delivery, distribution, and control, such as motors, transformers, and converters, that can function at high frequencies and minimize energy loss. Low silicon steel, including Fe-3.5 wt%Si alloy, belongs to a class of materials that have been utilized in energy transformation devices for many years due to the favourable properties that include high permeability, low coercivity, and low cost. However, the electrical resistivity of low silicon steel alloys is not optimal for alternating current (AC) applications with frequencies exceeding 1 kHz due to the high eddy current losses [1]. High silicon electrical steel (HSES) is a material that was developed to address this issue by increasing the silicon content to 6.5 wt%, resulting in a higher electrical resistivity of approximately 81 μΩcm [2].

The conventional method of producing HSES involves carefully controlling the cooling rate to suppress the formation of brittle ordered phases with structures such as DO_3 and B2 that can lead to brittle mechanical failure. This often requires the use of toxic chemicals such as

* Corresponding author.
E-mail address: chtlee@ntu.edu.sg (C.H.T. Lee).
[1] contributed equally to this work.

https://doi.org/10.1016/j.matdes.2025.113730
Received 6 December 2024; Received in revised form 13 February 2025; Accepted 13 February 2025
Available online 14 February 2025

$SiCl_4$ that pose a risk to both human health and the environment. The development of HSES using chemical vapor deposition (CVD) addressed this limitation. Notably, the CVD method avoids the formation of brittle DO_3 and B2 phases [3] in preference for the disordered A2 phase that offers better mechanical properties compared to those brittle phases.

In response to the need for energy-efficient devices, melt spinning of HSES has been developed, producing thin sheets that meet the requirements of the lamination structure of electrical motors [4]. Subsequent development of the melt spinning methods resulted in significant advances in the production of energy-efficient devices, making them more environmentally friendly and cost-effective. This method represents a significant advance compared to the conventional fabrication process, which requires precise cooling rates to suppress the formation of brittle ordered phases. Ongoing research is likely to lead to further improvements in the properties and production methods of HSES.

In order to assess the total iron losses in electrical steels (ES), it is typically necessary to minimize both hysteresis and eddy current losses. Hysteresis losses depend on a number of factors, including grain size, crystallographic texture, chemical ordering, and intrinsic material properties such as magneto-crystalline anisotropy, coercivity, and saturation magnetization [5]. In the manufacturing process of ES using cold/hot rolling, Goss texture (the (110) planes of the crystal lattice align parallel to the rolling direction, and the [0 0 1] direction is also aligned with the rolling direction) is obtained to reduce hysteresis loss, as the ⟨0 0 1⟩ direction represents the easiest magnetization direction in the cubic crystallographic system. Our previous work [6–8] has shown that laser powder bed fused Fe-3.5 wt% Si exhibits an extremely strong λ-fiber texture ((0 0 1)//BD), but it is still unclear whether this texture is present in laser-directed energy-deposited Fe-Si alloy. Additionally, post-annealing can result in abnormal grain growth (ABG) with Goss-oriented grains along the rolling direction, which can improve magnetic performance and reduce hysteresis loss. In a recent study by Fang et al [9], ABG was successfully induced with grain sizes > 4 cm, high magnetic flux density of $B_{50} = 1.87$ T with iron loss $P_{1.5T/50Hz}$ as low as 4.1 W/kg. The point of interest in the present study was whether the thermal annealing process can induce Goss-oriented ABG in laser-directed energy-deposited Fe-Si alloys.

Conventionally, the most direct way to reduce eddy current loss is by introducing an electrically insulated layer as used in soft magnetic composites (SMCs) [10]. With a variety of coating methods such as ball milling [11], surface oxidation [12], chemical deposition [13], sol–gel [14], organic coatings (e.g. Epoxy, Acrylic, Polyester, etc.) or inorganic coatings (e.g. Alumina, Silica) were deposited onto ferromagnetic particles (e.g Fe-Si, Fe-Ni, or Fe-Co). High-pressure compaction followed, to form prototype shapes. Since this process induces non-conductive phases, the static magnetic performance (such as permeability) is weakened but the dynamic response is improved leading to lower core energy losses in the high-frequency range.

Additionally, to reduce eddy current loss in additively manufactured ES, one solution is to build thin components such as the Hilbert structure investigated by Plotkowski et al. [15], and geometric design [16]. In addition, since we found that second amorphous phases can be formed during L-PBF, it is worth exploring whether we can utilize this second phase transformation to create thin walls with non-conductive phases to further reduce eddy current loss after annealing.

Researchers have been exploring additive manufacturing methods, such as laser powder bed fusion (L-PBF), electron beam powder bed fusion (EB-PBF), and direct energy deposition (DED) techniques, for fabricating HSES in addition to melting spinning. Garibaldi [17] investigated the metallurgical microstructure of laser powder bed fused 6.8 wt%Si alloy and found that its permeability exhibited higher performance than JNEX-Core counterparts (a high-silicon steel sheet with a uniform silicon content of 6.5Si% throughout the sheet manufactured by JFE Steel Corporation, Japan). However, cracks remained a major concern in the printed samples [18]. On the other hand, EB-PBF was able to print HSES without any cracks by Yang et al. [19]. Porosity in the sample was found to result in lower iron loss, suggesting a new way to fabricate HSES, but this structure could not maintain or improve magnetic performance [20]. The integration of DED techniques for HSE was also reported in references [21]. The grain structure evolution during solidification and solid-state grain growth was influenced by DED process parameters (e.g., inter-pass timing and number of unidirectional passes), which highlights the novel ability to engineer grains spanning multiple layers. For the DED-manufactured Fe-6Si alloy, the magnetic performance was evaluated and microstructure was characterised which were reported by References [22,23]. However, for the core losses of additively manufactured FeSi alloy, there is a limited number of publications on the core losses of Fe-Si additive-produced parts, especially considering using the DED technique.

Innovative design strategies for electrical steels must balance conflicting requirements, such as reducing magnetic losses while maintaining high permeability and low coercivity. Our work introduces a novel approach of utilizing amorphous oxide-rich strips to reduce magnetic losses. This is achieved through a strategic annealing process that promotes the formation of Goss abnormal grain growth (ABG) and extensive amorphous oxide-rich strips (oxide inclusions) in 24 h of annealed HSES alloy, fabricated by a DED process. This unique microstructural feature not previously reported in laser-assisted DED Fe-Si alloy has been demonstrated to significantly reduce hysteresis and eddy current losses. The evolution of microstructure and the effects on the functional properties such as core losses at varied frequencies are investigated. The presence of silica has been reported in previous work [6] in the L-PBFed HSES alloy while not found in the conventional ES. As we know, Non-metallic inclusions are discrete, minute secondary phases that manifest within the microstructure of metal alloys due to the fabrication process. These inclusions are widely recognized for their propensity to compromise the mechanical properties of alloys [24]. However, the effects of oxide inclusions on the total core losses have been little reported. Herein, we present the magnetic and loss results of a recrystallized HSES alloy with Goss ABG and oxide inclusions. These findings pave the way for integrating additive manufacturing techniques with targeted thermal treatments to improve performance in high-frequency electrical applications, such as transformers and motors.

2. Experimental section

The pre-alloyed Fe-6.5 wt%Si powder raw material was commercially supported by Sailong, ltd, China, with the particle size distribution ranging from 45 to 105 μm. The additive manufacturing process was conducted using a laser-directed energy deposition machine (Optomec®, USA) equipped with a 400 W fiber laser in maximum power and 4 standard powder feeders The LENS process is conducted in an argon (purity: 99.999 %) purged chamber with oxygen level kept blew 10 ppm to prevent impurity pick-up during deposition. Optomec's proprietary powder-feed system was used to precisely flow small quantities of powder into the process. A striping deposition strategy was employed to fabricate a ring method on a stainless-steel substrate, as shown in Fig. 1a. The fabricated parts were built on a steel substrate with dimensions of 100 × 100 × 30 mm^3.

The samples were designed to have two different shapes for microstructure characterization and magnetic measurement purposes. The first shape was a cube with dimensions of 10 × 10 × 10 mm^3, while the second shape was a ring with dimensions of OD (outer diameter) 30 × ID (inner diameter) 26 × H (height) 10 mm^3, which was subsequently machined to OD 30 x ID 27 x H 8 mm^3. The density (ρ) of AP and 1000–24 samples are measured using the Archimedes method with values of 7390 kg/m^3 and 7180 kg/m^3.

The annealing process was conducted using a tube furnace with 99.99 % argon gas protection at temperatures of 1000 ℃ for 24 hrs, followed by furnace cooling. The abbreviated notations AP and 1000–24 were used to refer to the conditions of as-printed and the annealing process. Fig. 1e shows a schematic diagram that illustrates the annealing

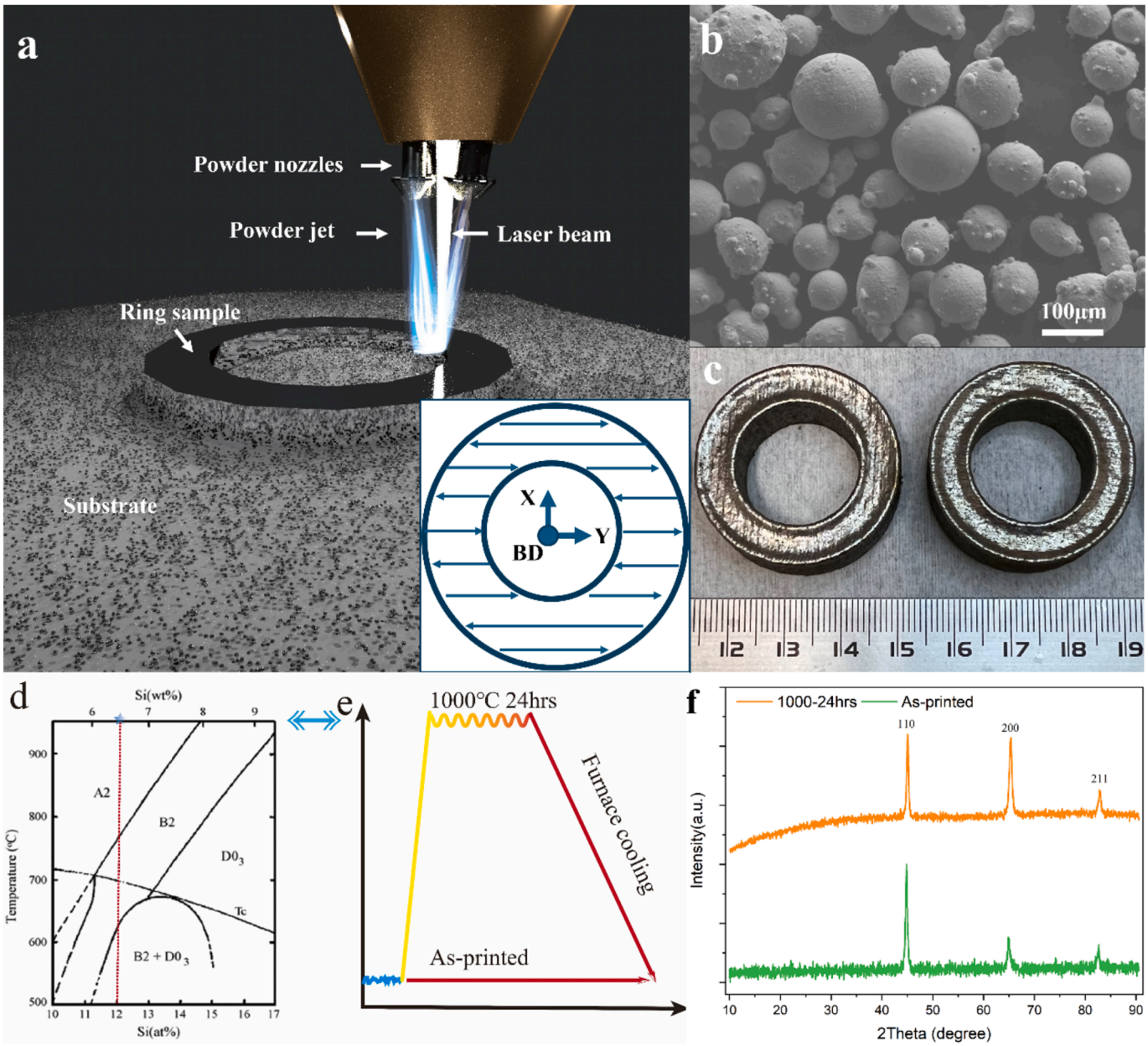

Fig. 1. LENS process and powder morphology: a)Schematic illustration elucidating the intricacies of the LENS procedure, encompassing the strip scanning methodology; b) SEM depiction capturing the intricate morphology of the pre-alloyed Fe-6.5Si powder; c)Visual representation showcasing the energy deposited rings, prior to the meticulous process of electrical-wire machining, earmarked for subsequent magnetic measurements; Annealing strategies aligned with Fe-Si phase diagram [25] (d) and (e) a schematic diagram further elaborating the annealing procedures, providing a visual representation of the phase diagram-guided methodologies; (f) X-ray diffraction patterns revealing disordered BCC phases within both the AP and 1000–24 specimens.

processing strategy used in this study, according to the Fe-Si phase diagram (Fig. 1f). The strategies involve heating the fabricated samples to 1000 ℃ temperatures (A2 phase zone) and holding them for 24 h, then followed with furnace cooling to obtain specific microstructural features. Before metallographic analysis, the fabricated samples were hot-mounted in conductive resin, progressively ground, and mirror-polished. The microstructure and texture of the printed samples were analysed using a Scanning Electron Microscope (SEM, 7800 FEG-SEM, JEOL, Japan) equipped with an Electron Backscatter Diffraction detector (EBSD, Symmetry S3, Oxford, UK) and an aberration-corrected scanning transmission electron microscope (AC-STEM, JEOL ARM300F, Japan). TEM samples were prepared using the Focus Iron Beam technique (FIB, Gemini 2 550, Zeiss, Germany) through milling and polishing procedures with currents of 30nA, 8nA, 100pA, and 20pA. The phases of AP and 1000–24 samples were determined by X-ray diffraction (XRD) using a Bruker D8 Advance diffractometer, configured in theta-2theta geometer, equipped with an X-ray tube with a Cu anode ($\lambda = 1.5406$ Å). 2theta ranges from 10° to 90°.

According to the ASTM Standard A927/A927M-11, ring-shaped samples coiled with copper wires (150:30, 1st: 2nd winding ratio) were subjected to AC-ring testing using a magnetometer (MATS-3000 M, Linkjoin, China) at room temperature and frequencies from 50 Hz to 500 Hz. At the frequency of 50 Hz, the applied magnetic field strength ranged from 200 A/m to around 3000 A/m. The quasi-static magnetic properties were measured using the direct current (DC) ring method using a magnetometer (MATS-2010D, Linkjoin, China) at room temperature. For electrical resistivity measurement, a 4-probe (4FPs) measurement system was employed. The bulk samples were cut into thin

thicknesses of 250 μm using electrical wire cutting, followed by grinding and polishing to remove surface oxidation and EMD effects. The samples were then measured using a 4FPs system at room temperature.

3. Results

3.1. Microstructural characterizations

The diffraction patterns acquired from Fe-Si alloys, both pre- and post-annealing, reveal the presence of three distinct and prominent peaks positioned at angles of 45°, 65°, and 83° as shown in the supplementary material, Fig. 1f. These angles correspond respectively to the crystallographic planes (110), (200), and (211) of the Fe body-centered cubic (BCC). Notably absent, however, is the discernible presence of the superlattice (001) characteristic of the B2/DO_3 ordered phase. This absence is consistent across both the as-printed (AP) sample and the 1000–24 sample, implying that the microstructural composition exclusively comprises a BCC phase. The evident obstruction of the ordered phase's formation within the AP sample can be primarily attributed to the rapid cooling rate encountered during the DED process. This high cooling rate hampers the progression toward the ordered phase. This is in sharp contrast to the customary approach of inducing the formation of ordered B2/DO_3 phases in high-silicon alloys, which typically necessitates a sequence of successive annealing steps. Intriguingly, our study adopts a departure from convention by employing only a solitary annealing step, thus failing to incite the emergence of the desired ordered B2/DO_3 phases even subsequent to the heat treatment procedure.

Furthermore, as depicted in Fig. 2a, and 1b, the utilization of precession electron diffraction (PED) proved instrumental in discerning the dual states of B2 order and disorder BCC (A2) phases. The phase contrast mapping presented in Fig. 2b demonstrates that the A2 phase permeates approximately 96.9 % of the total area within the AP sample, while the B2 phase is sparsely distributed, accounting for a mere 3.1 % diffusely. To gain a deeper insight, the atomic-resolution high-angle dark-field scanning transmission electron microscopy (HAADF-STEM) images were taken in the A2 phase region, with the zone axis aligned to (001). This investigative highlighted a (110) d-spacing of 2.11 Å, as portrayed in Fig. 2c. Supplementing the HAADF-STEM analysis, the corresponding Fast Fourier Transform (FFT) image noticeably lacks evidence of the (001) superlattice of the B2 phase (lattice measured 2.98 Å). Further insight was derived from Electron Energy Loss Spectroscopy (EELS) measurements, as illustrated in Fig. 2d. In the EELS findings, Silicon Kα loss peaks around ~1800 eV are absent, showing that the STEM image captures the atomic presence of iron (Fe) rather than the ordered phase.

In the microstructural examination of the 1000–24 sample, we present an atomic-resolution HAADF-STEM image taken along the [001] zone axis, as shown in Fig. 2e. The determined lattice parameter is denoted while the AP is represented as 2.98 Å. In the corresponding Fast Fourier Transform (FFT) image (Fig. 2e-1) and the corresponding Inverse Fast Fourier Transform (IFFT) image shows the interplanar crystal distance of (-110) is 2.03 Å, with the determined lattice parameter is 2.88 Å. There is a lattice mismatch between the AP and 1000–24 sample, which can be estimated by [26]:

$$\delta = 2\frac{a_1 - a_2 cos\theta}{a_1 + a_2 cos\theta} \tag{1}$$

Where a_1 and a_2 are the lattice parameters of the disordered and ordered phases respectively; θ is the angle between the two planes. The calculated lattice mismatch is 3.41 %.

The presence of superlattice diffraction spots indicates the existence of a short-range ordered phase (SROP) known as B2/DO_3. Moreover, we have generated an image of this SROP, (Fig. 2g). It appears that ordered domains, with dimensions less than 2 nm, are dispersed uniformly throughout the sample. Geometric Phase Analysis (GPA), was also performed, see Fig. 2h and Fig. 2i. The interface between the ordered and disordered domains reveals a substantial disparity in strain along the x and y directions, signifying a lattice misfit between the ordered and disordered phases. This misfit induces elastic strains due to the mismatch in atomic radius between Si and Fe atoms, leading to the

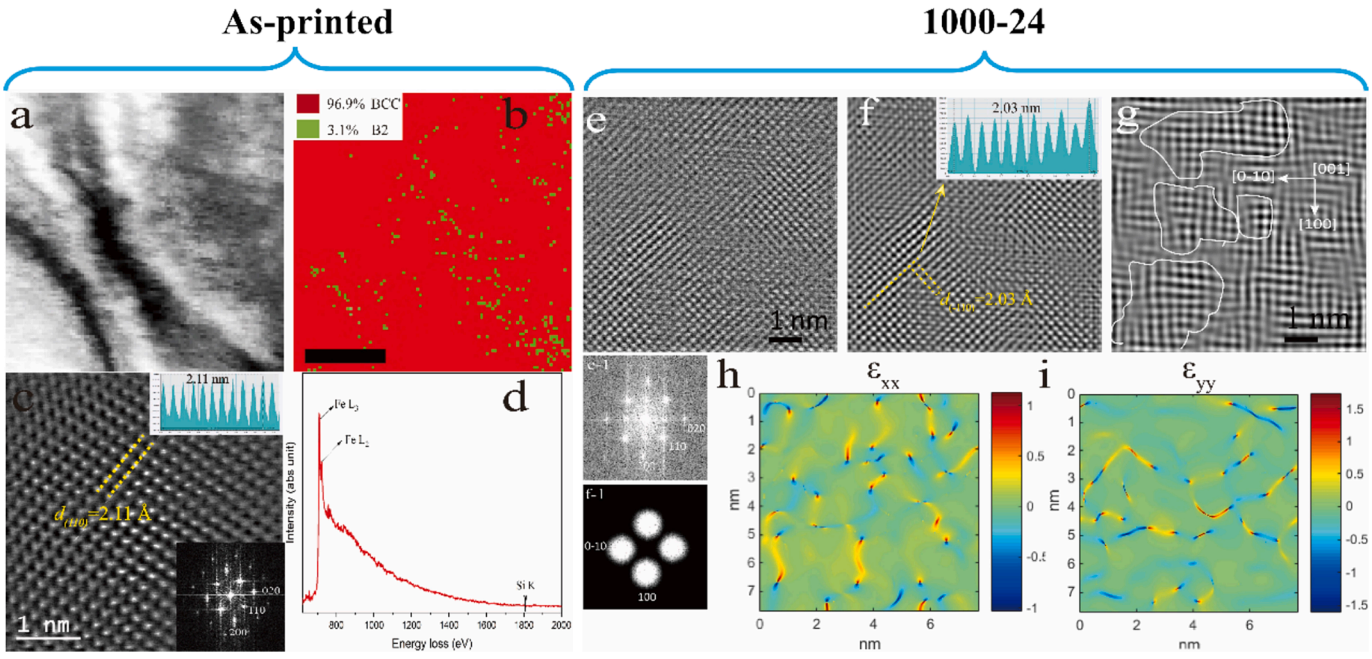

Fig. 2. Micro-level analysis using PED technique: (a)virtual brightfield mapping (b) phase contrast mapping, scale bar is 500 nm; (c) The atomic-level resolution HAADF STEM image insight into AP revealing atomic lattice structure. The insert depicted herein presents the FFT diffractogram of the complete spatial domain, offering valuable insight into chemical ordering. Notably, the FFT diffractogram reveals an absence of discernible alternating intensity fluctuations, thereby indicating the conspicuous absence of an ordered B2 phase. Notably, the lattice parameter measures 2.98 Å, and (d) complementary EELS results show the absence of Si Kα edge; Evidence of short ordering in 1000–24 sample: (e) Atomic resolution HAADF-STEM image of the 1000–24 sample: (f) super lattice FFT filtered image. (e-1) corresponding FFT image of (e); (f-1) corresponding FFT image of (f); GPA results of strain tensor ε_{xx} (h) and ε_{yy} (i); The lattice parameter of 1000–24 is 2.88 Å.

tensile (positive, yellow) strain caused by Si, while nearby regions exhibit compressive (negative) strain [27]. In the GPA, lattice distortion can be observed at the interface between the ordered and disordered phase.

The magnetic attributes of electrical steels exhibit a profound sensitivity to the orientation of texture. Consequently, electron backscatter diffraction (EBSD) was used to show grain orientations inherent within the 1000–24 and AP samples. The interplay between texture orientation and microstructure in the AP and 1000–24 samples is seen in Fig. 3. Within the AP microstructure, wavey structures are discernible and aligned with laser tracks from the DED process. The dominant texture orientation within the AP sample corresponds to (001)//BD texture. Conversely, the 1000–24 sample shows Goss abnormal grain growth (Goss ABG), in both top-view (Fig. 3c) and side-view (Fig. 3d). This Goss ABG texture could underpin the enhancement of magnetic properties and reduction in hysteresis losses.

3.2. Soft magnetic properties

Fig. 4, shows the quasi-static magnetic performance of AP and 1000–24. In Fig. 4a and 3b, the initial polarization vs magnetic field strength, $J-H$ and relative permeability vs magnetic field strength, μ_r-H curves for the AP and 1000–24 cases are presented together with fitted analytical models. The three-parameter analytical model is commonly used to link the measured J-H curve properties with finite element method (FEM) simulations [28].

$$\frac{H}{H_0}=\frac{J}{J_0}+\left(\frac{J}{J_0}\right)^{u-1} \tag{2}$$

where, $J_0, H_0,$ and u are three fitting parameters used to fit the measurement J-H data. The results of these fitting parameters are listed in Table 1. By rearranging Eq. (2), the relative permeability can be obtained as:

$$\mu_r=\frac{J_0}{H_0\mu_0\left[1+\left(\frac{J}{J_0}\right)^{u-1}\right]} \tag{3}$$

Specifically, the peak magnetic polarization (J_p) for the 1000–24 sample, at an applied magnetic field strength of 3000 A/m, is found to be 1.031 T. This is 20.4 % lower than its AP counterpart, which registers at 1.295 T.

This smaller value can be attributed to the formation of oxides inside the microstructure that inhibit the motion of domain walls. Quasi-static maximum relative permeabilities, $\mu_r max$ were measured to be 931.6 for the 1000–24 samples and 909.7 for the AP sample giving only a 2.38 % difference. Fig. 4c presents the quasi-static J-H hysteresis loops of the AP and 1000–24 samples. The quasi-static coercivities of 1000–24 and AP were measured at 15.41 A/m and 53.64 A/m respectively, demonstrating a 71.2 % improvement after annealing. It is noteworthy to mention that the quasi-static coercivity H_c, depends on structural ordering, grain size, stresses, and pinning forces that lattice defects exert on domain wall motion [29–31]. The reduced H_c in the 1000–24 samples can be attributed to the relief of residual stresses, an increase of the average grain size, and the reduced magneto-crystalline anisotropy, thus a softer magnetic response [32]. It is known from previous studies, that the decrease of magneto-crystalline anisotropy is due to high silicon levels [32]. Fe-Si alloys with Si concertation below 3 wt% exhibit a magneto-crystalline anisotropy higher than ~0.38×10^6 erg/cm^3, while concertation of 6.5 wt% presents ~0.22×10^6 erg/cm^3. Curie Temperature also decreases with increasing Si content [32]. The lattice

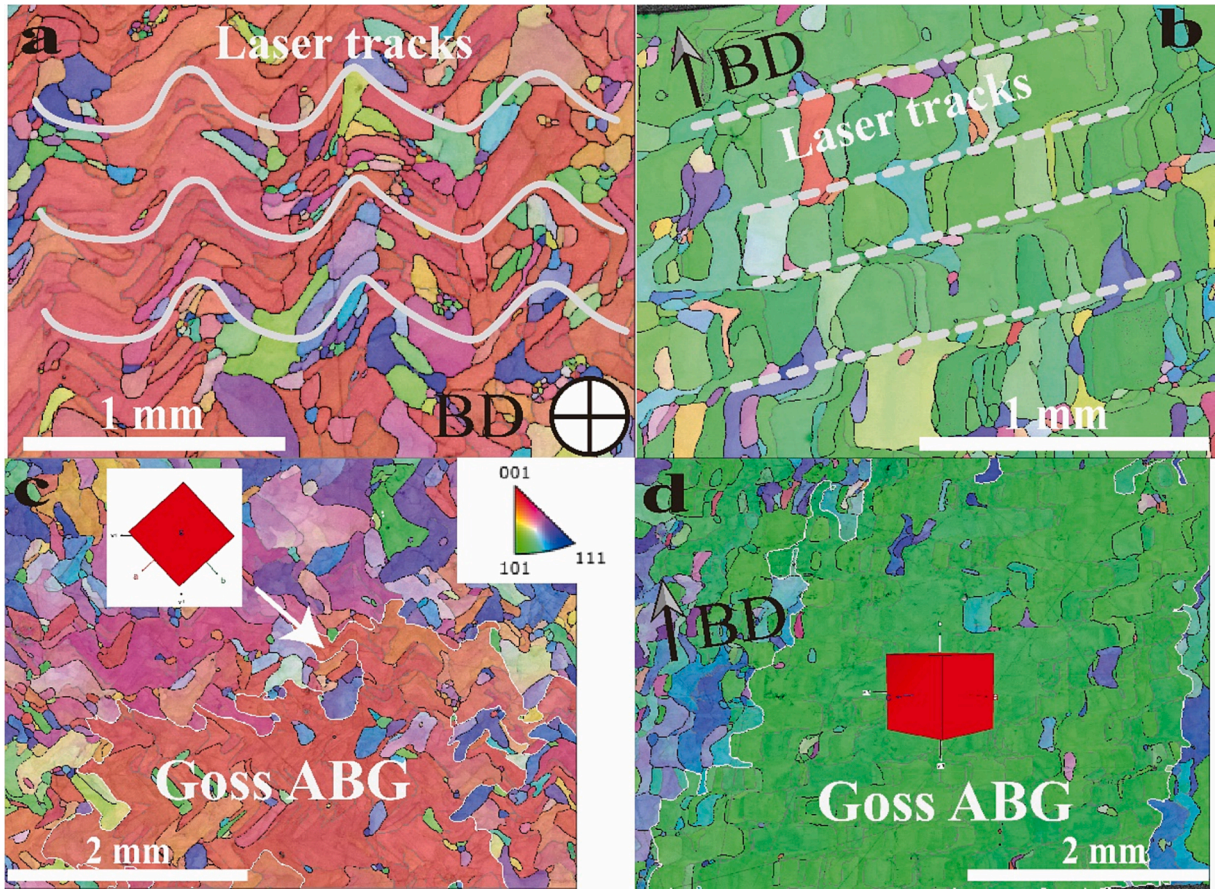

Fig. 3. EBSD (IPF-Z colouring) results show the crystallographic orientation of AP (a: top-view) (b: side-view) and 1000–24 (c: top-view) (d: side-view) samples.

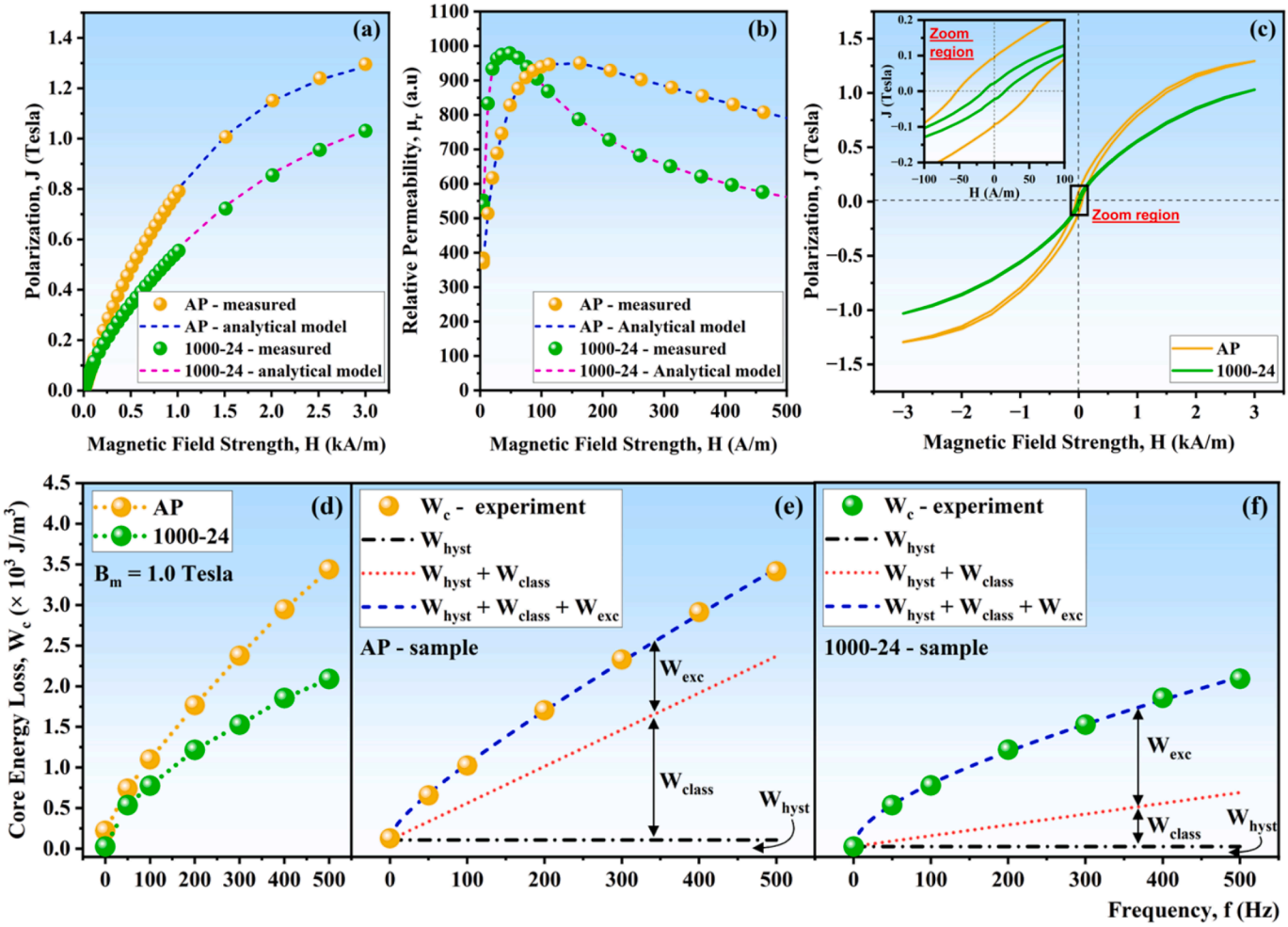

Fig. 4. Quasi-static magnetic properties of AP and 1000–24 samples: (a) Initial magnetization curves; (b) Relative permeability vs magnetic field strength; (c) Quasi-static J-H hysteresis curves; Core energy loss behaviour of AP and 1000–24 samples at a peak flux density of $J_p = 1T$ from quasi-static state to 500 Hz: (d) Measured core energy losses (W_c), (e) Separation of core energy losses into hysteresis losses (W_{hyst}), classical losses (W_{class}), and excess losses (W_{exc}) for AP and (f) 1000–24.

Table 1
Fitting parameters for the initial J-H curve (H = 3000 A/m).

Sample	J_o	H_o	u
AP	22	0.7580×10^6	0.7×10^3
1000–24	21	0.7590×10^6	0.8×10^3

constant for ordered Fe-6.5wt.%Si is ~2.849 Å [33,34] compared to the ~2.98 Å on the AP state. All the aforementioned factors contribute to the softer magnetic response of the 1000–24 sample. For magnetic material, coercivity and permeability can be described by the Grain Size Dependence of Coercivity and Permeability (GSDCP) theory [35–39]. The GSDCP theory shows that the coercivity agrees with the grain size D^{-1} law for particle sizes larger than the domain wall width (δ_w). Based on GSDCP H_c, can be described by [39]:

$$H_c = p_c \frac{\sqrt{A_{ex}K_1}}{J_s D} \quad (\delta_w < D) \tag{4}$$

Where D is the average grain size [μm]; K_1 is the magneto-crystalline anisotropy [erg/cm^3]; J_s is the saturation polarization [T];, p_c is a dimensionless factor; $A_{ex} = k_B T_c / 2\alpha_0$ is the exchange constant; k_B is Boltzmann's constant; T_c is the Curie temperature [K]; α_0 is the lattice constant [Å]; $\delta_w = \pi(A_{ex}/K_1)^{1/2}$ is the domain wall width [μm]. Therefore, based on GSDCP, the following beneficial effects of annealing on the overall H_c can be defined: 1) increased grain size; 2) reduced magneto-crystalline anisotropy. This combination of parameters yields a softer magnetic response for the 1000–24 sample. Fitting parameters for the coercivity of the 1000–24 sample are presented in Table 2:

Furthermore, low values of polarization remanence J_r, were observed due to the oxide inclusions embedded in the ferromagnetic matrix. The values of J_r were 0.0235 T and 0.0927 T for the 1000–24 and AP samples respectively.

The hysteresis core energy loss (W_{hyst}) is the energy loss per unit volume for the magnetic cores during a single magnetization cycle and can be obtained by measuring the area of the quasi-static hysteresis loop

Table 2
GSDCP theory coercivity fitting parameters for the 1000–24 sample.

Parameters	Symbols	Values
Dimensionless factor	p_c	0.5483
Magneto-crystalline anisotropy	K_1 [erg/cm^3]	0.22×10^6 [32]
Boltzmann's constant	k_B [J/K]	1.38065×10^{-23}
Curie temperature	T_c [K]	~968 [32]
Polarization saturation	J_s [T]	~1.8 [1]
Lattice constant	α_0 [Å]	2.88×10^{-10}
Average grain-size	D [μm]	> 40,000
GSDCP model $\left(H_c = p_c \frac{\sqrt{A_{ex}K_1}}{J_s D}\right)$		
Exchange stiffness constant	A_{ex}	2.32×10^{-11}
Domain wall width	δ_w [μm]	0.03226
Coercivity	H_c [A/m]	15.41

(Fig. 4c) at the applied magnetic field strength of 3000 A/m. The resulting values are 206.9 J/m^3, and 19.02 J/m^3 for the AP and 1000–24 samples. To investigate the dynamic core energy losses, sinusoidal waves with frequencies spanning from 50 Hz to 500 Hz were used, at peak polarization $J_p = 1$ T, Fig. 4d. The core energy loss associated with the AP sample exceeds that of the 1000–24 sample at all frequencies. The contrast is particularly pronounced at 500 Hz, where the core energy loss of the AP sample is 39.2 % higher than that of the 1000–24 sample.

It is of interest to separate the contributions to core energy losses into three components using Bertotti's statistical model [40–42]. The component losses: Hysteresis (W_{hyst}), classical eddy current (W_{class}), and excess losses (W_{exc}). The sum can be written as:

$$W_c = W_{hyst} + W_{clas} + W_{exc} \tag{5}$$

The hysteresis core energy loss, W_{hyst} is the energy loss per unit volume for the magnetic cores during a single magnetization cycle, and can be obtained by measuring the area of the quasi-static hysteresis loop as stated below [1,40–42]:

$$W_{hyst} = \oint \frac{J}{\mu_0 \mu_r} dJ = C_{hyst} J_p^{\alpha} \tag{6}$$

Where C_{hyst} and α are coefficients. In the case of $J_p = 1T$, α is negligible.

In the range of frequency where the skin effect is negligible (up to kHz), dynamic losses depend on the component thickness, electrical conductivity, and mass density [1,40–42]:

$$W_{class} = \frac{\pi^2 \bullet \sigma \bullet d^2 \bullet J_p^2 \bullet f}{6 \bullet \rho} \tag{7}$$

Here, σ is the electrical conductivity; d is the component thickness; J_p is the peak polarization; f is the frequency and, ρ is the density.

The excess core energy losses, W_{exc} originate from eddy currents, mainly caused by domain wall branching and bowing [43–45]. These can be obtained by subtracting the W_{hyst}, and W_{class} from W_c. Excess core energy losses depend on the frequency f, peak polarization J_p, the number of active magnetic objects, and the cross-section area S of the sample [46,47]. Thus, W_{exc} can be fitted by the formula [40–42]:

$$W_{exc} = 8\sqrt{\sigma G S V_0} J_p^{1.5} f^{0.5} \tag{8}$$

Where σ is the electrical conductivity; G is a dimensionless parameter that was determined by Bertotti [40] with the value 0.1356; S is the cross-section of the sample; and V_0 is an intrinsic material parameter dependent on microstructure.

Substituting Eqs. (6)–(8) into Eq. (5), the Bertotti model of the core energy losses in a soft magnetic material can be written as:

$$W_c = C_{hyst} J_p + \frac{\pi^2 \bullet \sigma \bullet d^2 \bullet J_p^2 \bullet f}{6 \bullet \rho} + 8\sqrt{\sigma G S V_0} J_p^2 f^{0.5} \tag{9}$$

giving:

$$W_c = C_{hyst} J_p + C_{class} f J_p^2 + C_{exc} f^{0.5} J_p^{1.5} \tag{10}$$

Where C_{hyst} is the hysteresis coefficient; C_{class} is the eddy current coefficient and, C_{exc} is the excess loss coefficient.

Eqs. (6) and (10) are similar therefore few identification relations can be provided:

These parameters were evaluated for both AP and 1000–24 and the results are shown in Fig. 4e and 3f. A good agreement is obtained at different operational frequencies. The respective core energy loss coefficients for each condition are presented in Table 3.

Consequently, a discernible demarcation between hysteresis (W_{hyst}), classical (W_{class}) and excess losses (W_{exc}) components is evidenced in Fig. 4e and Fig. 4f. Loss separation values derived from Bertotti's statistical model for AP and 1000–24 samples are presented in Table 4 and 5 respectively.

Table 3
Fitting parameters for Core Energy Losses ($W_c = C_{hyst} J_p + C_{class} f J_p^2 + C_{exc} f^{0.5} J_p^{1.5}$).

Coefficient	Symbol	AP	1000–24
Hysteresis losses coefficient	C_{hyst}	204.45	12.62
Classical e losses coefficient	C_{class}	4.42	1.23
Excess losses coefficient	C_{exc}	47.25	66.19

Turning our attention to the different loss components, within the frequency range spanning from 50 Hz to 500 Hz, W_{class} was more dominant for the AP sample compared to the 1000–24. This is attributed mainly to the lower electrical resistivity of the AP sample and the height of the electromagnetic component. Previous studies have shown the increase in height and cross-sectional area play an important role in the enlargement of eddy current losses [48,49]. The excess energy loss W_{exc} was greater in the 1000–24 sample, mainly due to microstructural factors, the abnormal grain growth gives rise to crystallographic orientations that may favour the easy or hard magnetization axis. This inevitably affected testing since the ring method was used (which is ideal for isotropic magnetic materials). Furthermore, the non-magnetic oxide inclusions did not fully isolate the ferromagnetic particles, leading to significant eddy currents [43–45].

It can be concluded that after annealing, the quasi-static H_c was reduced, leading to a significant decrease of W_{hyst}. Note, however, that while this strategy mitigates hysteresis energy losses, the inherent non-ferromagnetic characteristics contribute to a decrease in J_p and J_r during the magnetization process. Oxide inclusions embedded in the ferromagnetic matrix can impede the motion of the domain wall, affecting the magnetic properties directly [50]. This may explain the limited increase in permeability after annealing. The reason why the core energy loss, W_c, of the 1000–24 sample is less than that of the AP sample is due to abnormal grain growth, stress relief, and magneto-crystalline anisotropy constants. Similar mechanisms for inducing magnetic softness have been observed in different studies using other additively manufactured alloys [17,51,52].

3.3. Electrical properties

Electrical resistivity was explored using a 4-point probe measurement method, with the findings shown in Fig. 5. A comparative analysis of the electrical resistivity between the AP (median 105 μΩcm) and the 1000–24 samples (median 119 μΩcm) shows augmented electrical resistivity in the 1000–24 sample, attributed to the extended annealing process, consistent with the observed reduction in eddy current losses at medium and high frequencies.

Table 4
As-printed condition core energy loss separation (..$J_p = 1T$)

Frequency (Hz)	W_c – meas. (J/m^3)	W_{hyst} – calc. (J/m^3)	W_{class} – calc. (J/m^3)	W_{exc} – calc. (J/m^3)	W_c – calc. (J/m^3)	W_c –meas./ calc. Diff. (%)
Quasi-static	206.9	204.4	0.04	4.7	209.2	1.11
50	740.5	204.4	221.1	334.1	759.7	2.59
100	1099.3	204.4	442.2	472.5	1119.2	1.81
200	1764.8	204.4	884.4	668.3	1757.2	0.43
300	2376.0	204.4	1326.7	818.5	2349.6	1.11
400	2946.2	204.4	1768.9	945.1	2918.4	0.94
500	3436.9	204.4	2211.1	1056.6	3472.2	1.02

Table 5
1000–24 condition core energy loss separation ($J_p = 1T$).

Frequency (Hz)	W_c – meas. (J/m^3)	W_{hyst} – calc. (J/m^3)	W_{class} – calc. (J/m^3)	W_{exc} – calc. (J/m^3)	W_c – calc. (J/m^3)	W_c –meas./ calc. Diff. (%)
Quasi-static	19.0	12.6	0.01	6.6	19.3	1.58
50	535.6	12.6	61.7	468.0	542.3	1.25
100	776.9	12.6	123.3	661.9	797.9	2.69
200	1217.2	12.6	246.7	936.1	1195.4	1.79
300	1524.8	12.6	370.0	1146.4	1529.1	0.28
400	1853.9	12.6	493.4	1323.8	1829.8	1.30
500	2088.8	12.6	616.7	1480.1	2109.4	0.99

3.4. Elemental analysis for oxide inclusions

To elucidate the underlying factors at play, further analysis of the AP and 1000–24 samples was performed using Scanning Electron Microscopy (SEM) coupled with Energy Dispersive X-ray Spectroscopy (EDS), see Fig. 6. The SEM analysis of the AP sample revealed a consistent microstructure devoid of any precipitates or oxide inclusions. This was corroborated by EDS mappings, which displayed a uniform distribution of iron (Fe), oxygen (O), and silicon (Si) elements. In contrast, the 1000–24 sample exhibited a greater prevalence of crack-like features. Through EDS analysis (as shown in Fig. 6a-h) at the mesoscopic scale, these features were initially identified as oxide inclusions that developed after heat treatment. To achieve a more detailed characterization of the oxide inclusions, a TEM lamella was prepared from the 1000–24 sample using Focused Ion Beam (FIB) milling as shown in Fig. 4i and j. Fig. 4k features the HAADF-STEM image, accentuating a discernible contrast discrepancy between the amorphous phase (discernible by the accompanying FFT image as inserted) and the Fe-Si substrate. The insert (FFT image) in Fig. 6k illustrates the presence of an amorphous strip in the 1000–24 sample. The corresponding TKD-EDS maps delineate the spatial distribution of O, Fe, Cr, and Si, indicating a distinct separation pattern among these elements between the amorphous strip and the matrix. Through the integration of EDX maps encompassing O, Si, and Fe, it becomes evident that the periphery of the amorphous phase exhibits an enrichment of Si and O. Moreover, nanoparticles with enrichment of Cr and O indicate the formation of chromium oxides. Additionally, we conducted chemical characterization using electron energy loss spectroscopy (EELS) to confirm the nanoparticle is a FeCrO compound with the presence of O Kα, Cr L, and Fe L edges, as shown in Fig. 6m. In the EELS data from the amorphous strips, Si Kα and O Kα edges also illustrate the formation of Silicon Oxides within the strips while at the edge, the Fe L edge signal is strong.

This enrichment suggests the formation of silicon oxide along the periphery of the substrate. Collectively, these observations show that the amorphous oxygen-rich region acts as an effective conduction barrier, mitigating eddy current loss. This phenomenon, in turn, elucidates the observed augmentation in electric resistivity and the concomitant reduction in eddy current loss. However, while annealing mitigates eddy current loss, the inherent non-ferromagnetic characteristics contribute to a decrease in flux density during the magnetization process. On the other hand, oxide inclusions can impede the motion of the domain wall, impacting the magnetic properties directly [48], which explains the reduced maximum flux density. Compared to the steelmaking process, there is a significantly greater likelihood of oxygen incorporation occurring at various stages, including raw material preparation, the DED process, and the annealing process. Initially, the oxidation of powder, arising from either gas atomization or storage, stands out as one of the primary sources contributing to the presence of oxygen in DED components [53]. Subsequently, within the DED process, as the temperature rises, interactions may form a solid solution in Fe resulting in a disordered BCC phase. Here, oxygen atoms can occupy octahedral and tetrahedral interstitial sites in the BCC unit cell, effectively serving as agents for solid solution hardening [54]. Oxide inclusions are observed to form within the material and at intergranular locations within the 1000–24 samples. This observation strongly suggests the absence of surface oxidation during the annealing process. Variations in the distribution of silicon oxides could potentially arise from distinct diffusion rates within different steel grades. In such a scenario, the diffusion rate of silicon in the HSES would prove adequate for generating layers with a banded structure. Airaksinen et al. [55] performed high-temperature

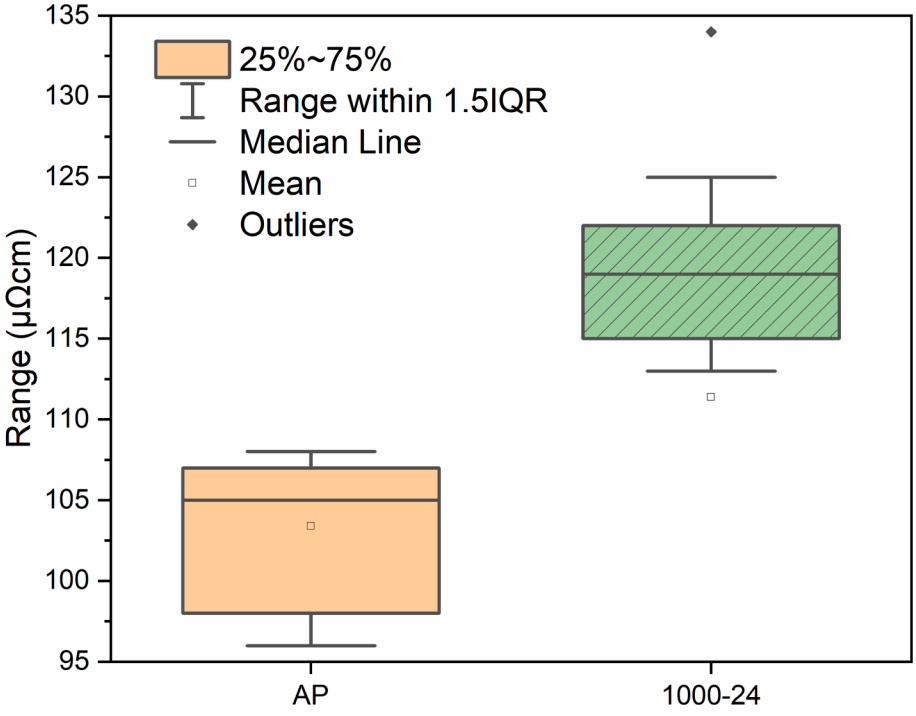

Fig. 5. Electrical resistivity of AP and 1000–24 samples tested by 4-point measurement.

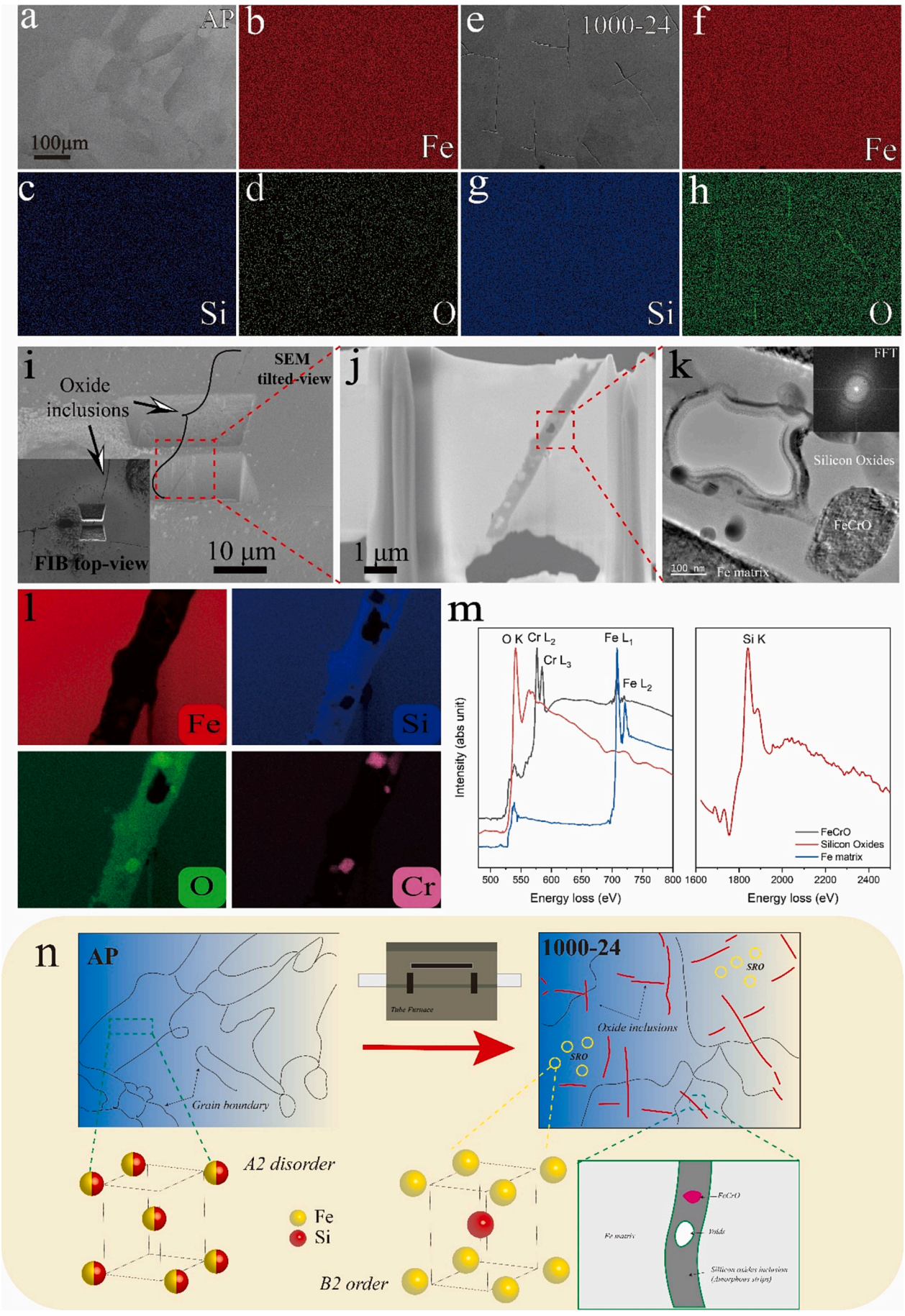

(caption on next page)

Fig. 6. SEM images illustrating the microstructure of AP (a-d) and 1000–24 (e-h) samples with responding Fe, Si, and O EDS distribution mappings; SEM/TEM images of 1000–24 (i-k), corresponding elemental distribution images (Fe, Si, O, and Cr) measured by EDS (l) and EELS data (m); (n) The schematic diagram of this investigation. On the top-left-hand part, the Fe-6.5 wt%Si alloy is fabricated via DED. The AP sample consists of the disorder BCC phase. By applying a subsequent annealing treatment (1000–24) as shown on the top-left-hand part, the SRO phase is formed with the accompanying formation of "crack-like" silicon oxides amorphous strips.

annealing experiments on EN 14622 and EN1.4828 stainless steels, revealing the internal formation of silicon oxide inclusions within these specific steel grades. Similarly, Lou et al [56] also identified intergranular inclusions within fully recrystallized stainless steel produced through additive manufacturing techniques. One plausible hypothesis for the formation of oxide inclusions can be proposed: As illustrated in Fig. 2h and Fig. 2i, the interface between ordered and disordered domains where is the stress concentration area. A stress contour consists of compressive and tensile strains as indicated by red and blue colours which are located at the interface between order and disorder domains, indicating the stress concentration places which can be considered as the crack's initial site. The lattice mismatch can potentially induce internal cracks due to lattice constant disparities. These internal cracks or voids (Fig. 6k) subsequently underwent oxidation, serving as the nuclei for the formation of oxide inclusions. Throughout the annealing procedure, these initial "cracks" tended to propagate intergranularly, leading to the expansion of such features. The schematic diagram of this work is shown in Fig. 6n. The synergistic mechanism for the decrease of W_{hyst} in the 1000–24 samples compared to the AP samples is the formation of ABG, process-induced residual stress relief, and minimization of the total demagnetization factor. In heterogeneous soft magnetic materials, an inner demagnetizing field arises, which reduces the applied field H_0 to $H_{int} = H_0 - NM$ (the inner magnetic field in the specimen is H_{int}, the demagnetization factor is N and the magnetization is M). The demagnetization factor N_{total} of a soft magnetic heterogeneous material depends on the inner demagnetization factor N_i(depending on grain size, grain boundary density, and non-magnetic inclusion distribution) and the external, geometric demagnetization factor N_e (depending on the shape of the specimen). The total demagnetization factor is the sum of the inner and external demagnetization factors: $N_{total} = N_i + N_e$ [57,58]. The external demagnetization factor can be determined by comparing a hysteresis curve from a soft magnetic heterogeneous material with a homogeneous material. A homogeneous material possesses a significantly larger hysteresis curve slope at small magnetization M with an almost zero inner demagnetization field, compared to a heterogeneous material. By estimating the angle ϕ between the heterogeneous and the homogeneous hysteresis curves at low magnetization M, N_{total} can be calculated by $\tan(\varphi) = H/M = N_{total}$ [58]. The inner demagnetization factor that occurs in a heterogeneous material, does not dependent on the sample's geometry. Since the 1000–24 samples consist of small oxidation channels randomly distributed through the soft magnetic matrix, their bodies don't consist of 100 % homogeneous soft magnetic material. Oxide inclusions represented non-magnetic gaps in the soft magnetic matrix, thus, creating an increase in the inner demagnetizing field. In this study, the introduction of ABG for the sample 1000–24, led to better coercivity and permeability, following the micromagnetic theory of the GSDCP model [35–38]. At the same time, an increase in the total demagnetization factor occurred due to oxide inclusions inside the soft magnetic matrix, and an increase in the oxide percentage content due to thermal post-processing. This combination of microstructural features acted as a deteriorating mechanism to the overall quasi-static magnetic performance. At the same time, due to ABG after annealing, the grain boundary density in the 1000–24 samples decreased compared to the AP ones. This induced a smaller inner demagnetization factor due to a decreased percentage of oxide inclusion on the grain boundaries, thus enhancing the final quasi-static magnetic performance of the 1000–24 samples. Additionally, process-induced residual stresses were eliminated after heat treatment, increasing further the positive contribution on the quasi-static performance [8,51,59,60].

4. Discussion

The presented research delves into the realm of HSES fabrication, which is crucial for advancing energy-efficient devices in modern society. Through innovative manufacturing methods, such as DED and meticulous heat treatment, the study achieved a significant reduction in both hysteresis and eddy current losses, which are pivotal factors in enhancing the performance of electrical steel. Notably, the investigation delves into the intricate microstructural evolution of the material, revealing the formation of ABG and the presence of extensive oxide inclusions, which play pivotal roles in reducing losses and improving magnetic properties. Goodall et al. [61] investigated the use of stochastic cracking in Fe-6.5 wt%Si soft magnetic material through additive manufacturing to reduce losses in electrical machines. The crack density and orientation are controlled by manipulating the scan strategies and speeds to increase the effective electrical resistance. The cracked samples exhibit lower losses, higher stacking factors, and potential applications in electric machine design, with the need for further analysis of the mechanical properties and fatigue behaviour. Tiisums et al. [62] explore the direct current (DC) magnetic properties of additively manufactured soft magnetic materials compared to traditional non-oriented electrical steels. The results indicated that the printed material exhibited lower hysteresis losses than conventional materials, with the introduction of air gaps in the material topology contributing to reduced AC losses. However, the complex topology of air gaps could increase the burden of the 3D printer, leading to the possibility of a manufacturing failure. To better understand the magnetic properties of the current Fe-6.5 wt%Si alloy, we summarized data including quasi-static coercivity and core losses of Höganäs SMCs and existing LPBF-printed Fe-Si alloy, as shown in Fig. 7. Compared with the Fe-3.5 wt% Si alloy, the current alloy exhibited lower coercivity and lower core losses. The losses can reach a level similar to SMC materials, or even lower than that of SMC materials. In addition, the coercivity of the proposed Fe-6.5 wt%Si is comparable to Fe-6.9 wt%Si alloy, although it is slightly inferior to the Fe-6.9 wt%Si alloy fabricated by L-PBF. The unique properties of Fe-Si alloys processed by L-DED stem from their lower cooling rates (10^2-10^4 K/s) and larger melt pool, leading to coarser, heterogeneous microstructures with columnar and equiaxed grain. In contrast, L-PBF's rapid cooling (10^3-10^8 K/s) produces finer, uniform grains with preferential orientations (e.g. $< 100 >$), enhancing coercivity, and saturation magnetization. But higher rapid cooling normally will result in larger residual stress which could hinder magnetic domain wall movement. L-DED's coarser grains increase Goss ABG formation in the annealed L-DED samples, which is more pronounced due to the larger grain sizes achievable in bulk L-DED builds. This contrasts with the finer grain structures typically seen in L-PBF alloys.

This work extends beyond previous research by offering a comprehensive understanding of the synergistic effects between the microstructure and losses, shedding light on the mechanisms underlying loss reduction in HSES. The findings have profound scientific implications, as they not only contribute to the fundamental understanding of magnetic materials but also pave the way for the development of more efficient and environmentally sustainable energy transformation devices. However, the effects of grain coarsening and amorphous strips on the mechanical properties were not investigated, which could be detrimental to the application of this material in the industry.

In summary, we successfully designed a novel HSES alloy via DED and feasible heat treatment, which exhibits a special microstructure consisting of ABG grains and silicon oxide amorphous strips. This study

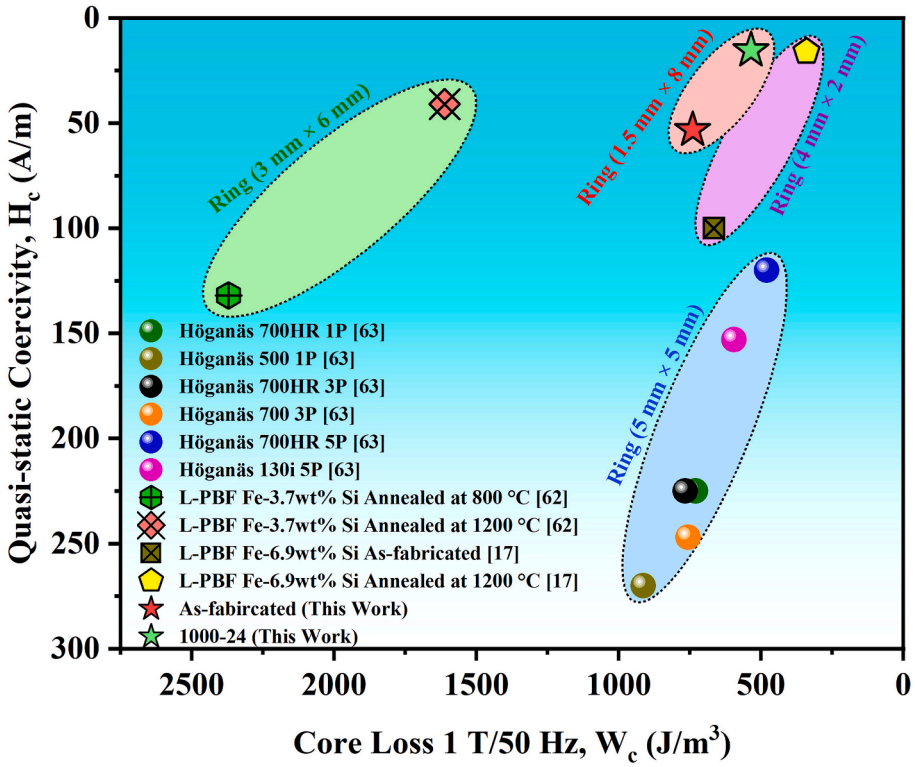

Fig. 7. Comparison of core loss at 1 T/50 Hz versus quasi-static coercivity of Höganäs SMCs and other Fe-Si alloy fabricated via LPBF [17,62,63] with Fe-6.5 wt%Si fabricated in this work.

underscores the immense potential of additive manufacturing techniques and tailored heat treatment processes in revolutionizing the design and performance of electrical steels, thus ushering in a new era of energy-efficient technologies with far-reaching implications for various industrial sectors.

5. Conclusion

In this study, we present a comprehensive exploration that establishes the viability of employing laser-engineered net shaping as an efficacious fabrication methodology for crafting high-silicon electrical steel and introduces an uncomplicated heat treatment aimed at reducing eddy current and hysteresis losses. This reduction is achieved through the synergistic effects of Goss abnormal grain growth (ABG) and the intricacies of internal oxide segregation. The magnetic attributes of both the as-prepared (AP) and 24-hour annealed (1000–24) samples were measured, with the following key findings:

1. The 1000–24 annealed sample showed reduced peak polarization J_p and markedly reduced coercivity H_c compared with the AP sample. Also, the hysteresis loss W_{hyst} of the 1000–24 sample was reduced to about a quarter of that of the AP sample, and dynamic core energy loss was reduced by about 39.2 %. Bertotti's statistical model was employed successfully to fit the total core energy loss and derive different loss components, such as hysteresis, classical eddy currents, and excess losses.
2. The microstructural evolution due to annealing illustrates the formation of Goss ABG, increasing magneto-crystalline anisotropy constants, which can be seen as the positive reason for the reduction of the hysteresis losses in the 1000–24 sample. Additionally, nonmagnetic oxide segregation was found in the 1000–24 sample which increases the electrical resistivity by 11.8 % and reduces eddy current loss.
3. A 3.4 % lattice mismatch between AP and 1000–24 samples was found, resulting in stress-induced cracks and oxidation sites. The transformative emergence of silica and an amorphous oxygen-rich stratum changes the magnetic characteristics of high silicon steel, imbuing it with traits akin to soft magnetic composites. This remarkable transition is accompanied by increased electrical resistance due to the non-conductive secondary phase. Hence, this study not only unveils a pioneering avenue for diminishing eddy current losses but also a novel trajectory for industrial applications with an innovative approach that holds considerable promise for advancing industrial magnetic materials.

The findings of this study provide a pathway for designing high-performance soft magnetic materials by combining additive manufacturing techniques with controlled annealing processes. The formation of abnormal Goss grain growth (ABG) and oxide inclusions serves as a blueprint for engineering microstructures that mitigate core losses while maintaining favorable magnetic properties. These insights encourage the development of new fabrication techniques that enable precise control over grain orientation, texture, and inclusion formation. The implications extend to the design of energy-efficient devices, suggesting that tailored magnetic materials could enhance the performance of electrical systems operating at high frequencies.

CRediT authorship contribution statement

Xiaojun Shen: Writing – review & editing, Writing – original draft, Visualization, Validation, Resources, Methodology, Investigation. **Konstantinos A. Liogas:** Writing – review & editing, Writing – original draft, Methodology, Investigation. **Verner Soh Qun Liang:** Investigation. **Yung Zhen Lek:** Investigation. **Fanbo Meng:** Investigation. **Yiming Shen:** Formal analysis. **John E. Huber:** Writing – review & editing. **Roger C. Reed:** Writing – review & editing. **Pei Wang:** Resources. **Alexander M. Korsunsky:** Writing – review & editing. **Christopher H.**

T. Lee: Writing – review & editing, Supervision, Resources.

Declaration of competing interest

The authors declare that they have no known competing financial interests or personal relationships that could have appeared to influence the work reported in this paper.

Acknowledgment

We would like to acknowledge the Facility for Analysis, Characterization, Testing, and Simulation, Nanyang Technological University, Singapore, for use of their facilities. The work was supported by the Panasonic Industrial Devices Singapore Pte. Ltd, Singapore, under its Joint Lab Programme 04IDS001408C140, National Research Foundation (NRF) Singapore under its NRF Fellowship Grant NRF-NRFF12-2020-0003. The work is also supported by the Agency for Science, Technology and Research (A*STAR) of Singapore via the Individual Research Grant (Grant reference No. A20E7c0109).

Data availability

Data will be made available on request.

References

[1] G. Ouyang, X. Chen, Y. Liang, C. Macziewski, J. Cui, Review of Fe-6.5 wt%Si high silicon steel—A promising soft magnetic material for sub-kHz application, J. Magn. Magn. Mater. 481 (2019) 234–250, https://doi.org/10.1016/j.jmmm.2019.02.089.

[2] C. Zhou, H. Jiang, C. Liu, B. Yan, P. Yan, Microstructure features of high performance soft magnetic alloy Fe-3 wt.% Si prepared by metal injection molding, Mater. Chem. Phys. 273 (2021), https://doi.org/10.1016/j.matchemphys.2021.125068.

[3] S. Crottier-Combe, S. Audisio, J. Degauque, J.L. Porteseil, E. Ferrara, M. Pasquale, F. Fiorillo, The magnetic properties of Fe Si 6.5 wt% alloys obtained by a SiCl4-based CVD process, J. Magn. Magn. Mater. 160 (1996) 151–153, https://doi.org/10.1016/0304-8853(96)00144-8.

[4] G. Ouyang, B. Jensen, W. Tang, J. Schlagel, B. Hilliard, C. Pan, B. Cui, K. Dennis, D. Jiles, T. Monson, I. Anderson, M.J. Kramer, J. Cui, Near net shape fabrication of anisotropic Fe-6.5%Si soft magnetic materials, Acta Mater. 201 (2020) 209–216, https://doi.org/10.1016/j.actamat.2020.09.084.

[5] P. Ghosh, R.R. Chromik, B. Vaseghi, A.M. Knight, Effect of crystallographic texture on the bulk magnetic properties of non-oriented electrical steels, J. Magn. Magn. Mater. 365 (2014) 14–22, https://doi.org/10.1016/j.jmmm.2014.04.051.

[6] X. Shen, F. Meng, K.B. Lau, P. Wang, C.H.T. Lee, Texture and microstructure characterizations of Fe-3.5wt%Si soft magnetic alloy fabricated via laser powder bed fusion, Mater Charact 189 (2022) 112012, https://doi.org/10.1016/j.matchar.2022.112012.

[7] F. Meng, K.A. Liogas, K.B. Lau, Y. Deng, A.M. Korsunsky, P. Wang, X. Shen, C.H. T. Lee, The selection of scanning strategy and annealing schedule for the optimization of texture and magnetic properties of Fe-3.5 wt%Si alloy parts fabricated by laser powder bed fusion, Addit. Manuf. 97 (2025) 104614, https://doi.org/10.1016/j.addma.2024.104614.

[8] X. Shen, H. Sheng, Y. He, K.A. Liogas, K. Boon Lau, P. Wang, F. Meng, K. Chen, N. Jia, U. Ramamurty, C.H.T. Lee, Evaluation of microstructure, mechanical and magnetic properties of laser powder bed fused Fe-Si alloy for 3D magnetic flux motor application, Mater. Des. 234 (2023) 112343, https://doi.org/10.1016/j.matdes.2023.112343.

[9] F. Fang, Y.X. Zhang, X. Lu, Y. Wang, M.F. Lan, G. Yuan, R.D.K. Misra, G.D. Wang, Abnormal growth of 100 grains and strong Cube texture in strip cast Fe-Si electrical steel, Scr. Mater. 147 (2018) 33–36, https://doi.org/10.1016/j.scriptamat.2017.12.034.

[10] H. Shokrollahi, K. Janghorban, Soft magnetic composite materials (SMCs), J. Mater. Process. Technol. 189 (2007) 1–12, https://doi.org/10.1016/j.jmatprotec.2007.02.034.

[11] Z. Wu, X. Fan, J. Wang, G. Li, Z. Gan, Z. Zhang, Core loss reduction in Fe–6.5 wt.% Si/SiO 2 core–shell composites by ball milling coating and spark plasma sintering, J. Alloy. Compd. 617 (2014) 21–28, https://doi.org/10.1016/j.jallcom.2014.07.217.

[12] E.Y. Kang, Y.H. Chung, M.-R. Ok, H.K. Baik, Research on the surface oxidation procedure of Fe-base metallic glass during wet oxidation treatment, Mater. Sci. Eng. A 449–451 (2007) 159–164, https://doi.org/10.1016/j.msea.2006.02.311.

[13] Z. Luo, X. Fan, W. Hu, F. Luo, G. Li, Y. Li, X. Liu, J. Wang, Controllable SiO2 insulating layer and magnetic properties for intergranular insulating Fe-6.5wt.%Si/SiO2 composites, Adv. Powder Technol. 30 (2019) 538–543, https://doi.org/10.1016/j.apt.2018.12.004.

[14] Z. Yao, Y. Peng, C. Xia, X. Yi, S. Mao, M. Zhang, The effect of calcination temperature on microstructure and properties of FeNiMo@Al2O3 soft magnetic composites prepared by sol-gel method, J. Alloy. Compd. 827 (2020), https://doi.org/10.1016/j.jallcom.2020.154345.

[15] A. Plotkowski, K. Carver, F. List, J. Pries, Z. Li, A.M. Rossy, D. Leonard, Design and performance of an additively manufactured high-Si transformer core, Mater. Des. 194 (2020), https://doi.org/10.1016/j.matdes.2020.108894.

[16] A.D. Goodall, G. Yiannakou, L. Chechik, R.L. Mitchell, G.W. Jewell, I. Todd, Geometrical control of eddy currents in additively manufactured Fe-Si, Mater. Des. (2023) 112002, https://doi.org/10.1016/j.matdes.2023.112002.

[17] M. Garibaldi, I. Ashcroft, J.N. Lemke, M. Simonelli, R. Hague, Effect of annealing on the microstructure and magnetic properties of soft magnetic Fe-Si produced via laser additive manufacturing, Scr. Mater. 142 (2018) 121–125, https://doi.org/10.1016/j.scriptamat.2017.08.042.

[18] M. Garibaldi, I. Ashcroft, M. Simonelli, R. Hague, Metallurgy of high-silicon steel parts produced using Selective Laser Melting, Acta Mater. 110 (2016) 207–216, https://doi.org/10.1016/j.actamat.2016.03.037.

[19] J. Yang, Z. Fu, J. Ye, D. Kübrich, C. Körner, Electron beam-based additive manufacturing of Fe93.5Si6.5 (wt.%) soft magnetic material with controllable magnetic performance, Scr. Mater. 210 (2022) 114460, https://doi.org/10.1016/j.scriptamat.2021.114460.

[20] M.P. Haines, F. List, K. Carver, D.N. Leonard, A. Plotkowski, C.M. Fancher, R. R. Dehoff, S.S. Babu, Role of scan strategies and heat treatment on grain structure evolution in Fe-Si soft magnetic alloys made by laser-powder bed fusion, Addit. Manuf. 50 (2022), https://doi.org/10.1016/j.addma.2021.102578.

[21] A. Plotkowski, J. Coleman, C.M. Fancher, M.P. Haines, S.R. Whetten, A.B. Kustas, Grain Structure Evolution in Fe-6Si During Directed Energy Deposition, JOM 76 (2024) 1031–1043, https://doi.org/10.1007/s11837-023-06279-3.

[22] K. Sun, F. Li, C. Rong, L. Zuo, Direct energy deposition applied to soft magnetic material additive manufacturing, J. Manuf. Process. 84 (2022) 162–173, https://doi.org/10.1016/j.jmapro.2022.10.004.

[23] J.M. Adamczyk, S.E. Birchall, E.T. Rothermel, S.R. Whetten, E.J. Barrick, C. J. Pearce, R.E. Delaney, J.W. Pegues, K.L. Johnson, D.F. Susan, T.C. Monson, A. B. Kustas, Characterization of Fe-6Si Soft Magnetic Alloy Produced by Laser-Directed Energy Deposition Additive Manufacturing, JOM 76 (2024) 863–874, https://doi.org/10.1007/s11837-023-06293-5.

[24] A. Slagter, J. Everaerts, L. Deillon, A. Mortensen, Strong silicon oxide inclusions in iron, Acta Mater. 242 (2023) 118437, https://doi.org/10.1016/j.actamat.2022.118437.

[25] J.S. Shin, J.S. Bae, H.J. Kim, H.M. Lee, T.D. Lee, E.J. Lavernia, Z.H. Lee, Ordering–disordering phenomena and micro-hardness characteristics of B2 phase in Fe–(5–6.5%)Si alloys, Mater. Sci. Eng. A 407 (2005) 282–290, https://doi.org/10.1016/j.msea.2005.07.012.

[26] J. Ren, Y. Zhang, D. Zhao, Y. Chen, S. Guan, Y. Liu, L. Liu, S. Peng, F. Kong, J. D. Poplawsky, G. Gao, T. Voisin, K. An, Y.M. Wang, K.Y. Xie, T. Zhu, W. Chen, Strong yet ductile nanolamellar high-entropy alloys by additive manufacturing, Nature 608 (2022) 62–68, https://doi.org/10.1038/s41586-022-04914-8.

[27] X. Chen, Q. Wang, Z. Cheng, M. Zhu, H. Zhou, P. Jiang, L. Zhou, Q. Xue, F. Yuan, J. Zhu, X. Wu, E. Ma, Direct observation of chemical short-range order in a medium-entropy alloy, Nature 592 (2021) 712–716, https://doi.org/10.1038/s41586-021-03428-z.

[28] G. Mörée, M. Leijon, Review of Hysteresis Models for Magnetic Materials, Energies 16 (2023) 3908, https://doi.org/10.3390/en16093908.

[29] G. Herzer, Grain size dependence of coercivity and permeability in nanocrystalline ferromagnets, IEEE Trans. Magn. 26 (1990) 1397–1402, https://doi.org/10.1109/20.104389.

[30] R.H. Yu, S. Basu, Y. Zhang, A. Parvizi-Majidi, J.Q. Xiao, Pinning effect of the grain boundaries on magnetic domain wall in FeCo-based magnetic alloys, J. Appl. Phys. 85 (1999) 6655–6659, https://doi.org/10.1063/1.370175.

[31] T. Ochirkhuyag, S.C. Hong, D. Odkhuu, Enhancing magnetic anisotropy and stability of α''-Fe16N2 phase by Co and V co-substitution, AIP Adv. 11 (2021) 015227, https://doi.org/10.1063/9.0000068.

[32] M. Littmann, Iron and silicon-iron alloys, IEEE Trans. Magn. 7 (1971) 48–60, https://doi.org/10.1109/TMAG.1971.1066998.

[33] F. Huyan, R. Larker, P. Rubin, P. Hedström, Effect of Solute Silicon on the Lattice Parameter of Ferrite in Ductile Irons, ISIJ Int. 54 (2014) 248–250, https://doi.org/10.2355/isijinternational.54.248.

[34] B. Wang, G. Li, Y. Wang, Y. Su, H. Sun, Z. Guo, D. Zhang, Z. Dong, Characterization of the Fe-6.5wt%Si Strip with Rapid Cooling Coupling Deep Supercooled Solidification, ACS Omega 6 (2021) 25412–25420. https://doi.org/10.1021/acsomega.1c03367.

[35] R. Alben, J.J. Becker, M.C. Chi, Random anisotropy in amorphous ferromagnets, J. Appl. Phys. 49 (1978) 1653–1658, https://doi.org/10.1063/1.324881.

[36] G. Herzer, Grain structure and magnetism of nanocrystalline ferromagnets, IEEE Trans. Magn. 25 (1989) 3327–3329, https://doi.org/10.1109/20.42292.

[37] G. Herzer, Soft magnetic nanocrystalline materials, Scr. Metall. Mater. 33 (1995) 1741–1756, https://doi.org/10.1016/0956-716X(95)00397-E.

[38] G. Herzer, Anisotropies in soft magnetic nanocrystalline alloys, J. Magn. Magn. Mater. 294 (2005) 99–106, https://doi.org/10.1016/j.jmmm.2005.03.020.

[39] D. Xue, G. Chai, X. Li, X. Fan, Effects of grain size distribution on coercivity and permeability of ferromagnets, J. Magn. Magn. Mater. 320 (2008) 1541–1543, https://doi.org/10.1016/j.jmmm.2008.01.004.

[40] G. Bertotti, General properties of power losses in soft ferromagnetic materials, IEEE Trans. Magn. 24 (1988) 621–630, https://doi.org/10.1109/20.43994.

[41] G. Bertotti F. Fiorillo G.P. Soardo THE PREDICTION OF POWER LOSSES IN SOFT MAGNETIC MATERIALS J. Phys. Colloques 49 1988 C8–1915-C8-1919 10.1051/jphyscol:19888867.
[42] G. Bertotti, G. Di Schino, A. Ferro Milone, F. Fiorillo, ON THE EFFECT OF GRAIN SIZE ON MAGNETIC LOSSES OF 3% NON-ORIENTED SiFe, J. Phys. Colloques 46 (1985) C6–385, https://doi.org/10.1051/jphyscol:1985671.
[43] F.J.G. Landgraf, J.C. Teixeira, M. Emura, M.F. De Campos, C.S. Muranaka, Separating Components of the Hysteresis Loss of Non-Oriented Electrical Steels, MSF 302–303 (1999) 440–445, https://doi.org/10.4028/www.scientific.net/MSF.302-303.440.
[44] M. Amar, F. Protat, A simple method for the estimation of power losses in silicon iron sheets under alternating pulse voltage excitation, IEEE Trans. Magn. 30 (1994) 942–944, https://doi.org/10.1109/20.312453.
[45] E.A. Périgo, B. Weidenfeller, P. Kollár, J. Füzer, Past, present, and future of soft magnetic composites, Appl. Phys. Rev. 5 (2018) 031301, https://doi.org/10.1063/1.5027045.
[46] L. Dakova, J. Fuzer, S. Dobak, P. Kollar, Y. Osadchuk, M. Streckova, M. Faberova, R. Bures, P. Kurek, M. Vojtko, Analysis of Magnetic Losses and Complex Permeability in Novel Soft Magnetic Composite With Ferrite Nanofibers, IEEE Trans. Magn. 54 (2018) 1–6, https://doi.org/10.1109/TMAG.2018.2866814.
[47] A. Bordianu, O. De La Barriere, O. Bottauscio, M. Chiampi, A. Manzin, A Multiscale Approach to Predict Classical Losses in Soft Magnetic Composites, IEEE Trans. Magn. 48 (2012) 1537–1540, https://doi.org/10.1109/TMAG.2011.2172927.
[48] M.C. Kulan, N.J. Baker, K.A. Liogas, O. Davis, J. Taylor, A.M. Korsunsky, Empirical Implementation of the Steinmetz Equation to Compute Eddy Current Loss in Soft Magnetic Composite Components, IEEE Access 10 (2022) 14610–14623, https://doi.org/10.1109/access.2022.3148593.
[49] M.C. Kulan, N.J. Baker, K.A. Liogas, O. Davis, J. Taylor, Improved Core Loss Calculations in Soft Magnetic Composites Considering 3-D Magnetic Flux Density Vectors and Geometry Dependent Eddy Currents, in: 2023 IEEE International Electric Machines & Drives Conference (IEMDC), IEEE, San Francisco, CA, USA, 2023: pp. 1–7. https://doi.org/10.1109/IEMDC55163.2023.10238928.
[50] Q. Ren, L. Zhang, W. Yang, Effect of Oxide Inclusions on the Magnetic Properties of Non-Oriented Electrical Steel, Steel Research Int. 89 (2018) 1800047, https://doi.org/10.1002/srin.201800047.
[51] K.A. Liogas, K.B. Lau, Z. Wang, D.N. Brown, E. Polatidis, P. Wang, A.M. Korsunsky, Effect of heat treatment on the microstructure and magnetic properties of laser powder bed fusion processed equiatomic Co-Fe, Addit. Manuf. 67 (2023) 103499, https://doi.org/10.1016/j.addma.2023.103499.
[52] M.S.K.K.Y. Nartu, S. Dasari, A. Sharma, V. Chaudhary, S.M. Varahabhatla, S. A. Mantri, E. Ivanov, R.V. Ramanujan, N.B. Dahotre, R. Banerjee, Reducing coercivity by chemical ordering in additively manufactured soft magnetic Fe–Co (Hiperco) alloys, J. Alloy. Compd. 861 (2021) 157998, https://doi.org/10.1016/j.jallcom.2020.157998.
[53] X. Guo, H.-L. Huang, M. Zhu, K. Hariharan, S.-C. Chien, N. Huynh, J. Hwang, W. Windl, C.D. Taylor, E.J. Schindelholz, G.S. Frankel, Interstitial elements created via metal 3D printing, Mater. Today 66 (2023) 92–104, https://doi.org/10.1016/j.mattod.2023.04.020.
[54] C. Liu, J. Cui, Z. Cheng, B. Zhang, S. Zhang, J. Ding, R. Yu, E. Ma, Direct Observation of Oxygen Atoms Taking Tetrahedral Interstitial Sites in Medium-Entropy Body-Centered-Cubic Solutions, Adv. Mater. 35 (2023) 2209941, https://doi.org/10.1002/adma.202209941.
[55] S. Airaksinen, T. Tuovinen, T. Vuolio, A. Laukka, E.-P. Heikkinen, E. Riekki, T. Fabritius, Oxide Scale Formation of EN 1.4622 and EN 1.4828 Stainless Steels during Annealing and Descaling Behavior in Neutral Electrolytic Pickling, Steel Research Int. 93 (2022) 2100366, https://doi.org/10.1002/srin.202100366.
[56] X. Lou, P.L. Andresen, R.B. Rebak, Oxide inclusions in laser additive manufactured stainless steel and their effects on impact toughness and stress corrosion cracking behavior, J. Nucl. Mater. 499 (2018) 182–190, https://doi.org/10.1016/j.jnucmat.2017.11.036.
[57] T.H. Kahan, Recherches sur le champ démagnétisant structural des ferromagnétiques, J. Phys. Radium 5 (1934) 463–470, https://doi.org/10.1051/jphysrad:0193400509046300.
[58] E. Kneller A. Seeger H. Kronmüller Ferrimagnetismus, in: E. Kneller, A. Seeger, H. Kronmüller (Eds.), Ferromagnetismus: Mit Einem Beitrag Quantentheorie Und Elektronentheorie Des Ferromagnetismus 1962 Springer Berlin Heidelberg, Berlin, Heidelberg 10.1007/978-3-642-86695-1_6 68 90.
[59] F. Uzun, H. Basoalto, K. Liogas, M.F. Slim, T.L. Lee, C. Besnard, Z.I. Wang, J. Chen, I.P. Dolbnya, A.M. Korsunsky, Tomographic eigenstrain reconstruction for full-field residual stress analysis in large scale additive manufacturing parts, Addit. Manuf. 81 (2024) 104027, https://doi.org/10.1016/j.addma.2024.104027.
[60] F. Uzun, H. Basoalto, K. Liogas, J. Chen, I.P. Dolbnya, Z.I. Wang, A.M. Korsunsky, Voxel-based full-field eigenstrain reconstruction of residual stresses in additive manufacturing parts using height digital image correlation, Addit. Manuf. 77 (2023) 103822, https://doi.org/10.1016/j.addma.2023.103822.
[61] A.D. Goodall, L. Chechik, R.L. Mitchell, G.W. Jewell, I. Todd, Cracking of soft magnetic FeSi to reduce eddy current losses in stator cores, Addit. Manuf. 70 (2023) 103555, https://doi.org/10.1016/j.addma.2023.103555.
[62] H. Tiismus, A. Kallaste, A. Belahcen, M. Tarraste, T. Vaimann, A. Rassölkin, B. Asad, P., Shams Ghahfarokhi, AC Magnetic Loss Reduction of SLM Processed Fe-Si for Additive Manufacturing of Electrical Machines, Energies 14 (2021), https://doi.org/10.3390/en14051241.
[63] A.B. Höganäs, Somaloy Material Data (2016).